PHYSICAL REVIEW B **94**, 195153 (2016)

Seebeck coefficient in correlated low-dimensional organic metals

M. Shahbazi* and C. Bourbonnais†

Regroupement Québecois sur les Matériaux de Pointe, Département de physique,
Université de Sherbrooke, Sherbrooke, Québec, Canada J1K-2R1

(Received 18 September 2016; revised manuscript received 12 November 2016; published 29 November 2016)

We study the influence of inelastic electron-electron scattering on the temperature variation of the Seebeck coefficient in the normal phase of quasi-one-dimensional organic superconductors. The theory is based on the numerical solution of the semiclassical Boltzmann equation for which the collision integral equation is solved with the aid of the renormalization-group method for the electronic umklapp scattering vertex. We show that the one-loop renormalization-group flow of momentum and temperature-dependent umklapp scattering, in the presence of nesting alterations of the Fermi surface, introduce electron-hole asymmetry in the energy dependence of the anisotropic scattering time. This is responsible for the enhancement of the Seebeck coefficient with respect to the band T-linear prediction and even its sign reversal around the quantum critical point of the phase diagram, namely, where the interplay between antiferromagnetism and superconductivity and also the strength of spin fluctuations are the strongest. A comparison of the results with available data on low-dimensional organic superconductors is presented and critically discussed.

DOI: 10.1103/PhysRevB.94.195153

I. INTRODUCTION

In the past few years we have seen expanding interest in the Seebeck coefficient as a sensitive probe of fluctuations encased in the quantum critical behavior of correlated electrons. This has been exemplified both experimentally and theoretically for quantum critical points in heavy fermions [1–5] and pnictides [6] and for hole- [7–10] and electron-doped [11,12] cuprates. In organic superconductors like the Bechgaard salt $(\mathrm{TMTSF})_2X$ series, also known to exhibit quantum criticality, the measurements of the Seebeck coefficient have been the subject of numerous reports following their discovery [13–19] until very recently [20]. However, these works have found very little theoretical echo as to the possible part played by quantum fluctuations in the thermoelectric response seen in these correlated quasi-one-dimensional (quasi-1D) metals. This topic, which has remained essentially unexplored so far [21], will be the main focus of the present work.

The quantum critical behavior of the Bechgaard salts is known to result from the juncture of a declining spin-density-wave (SDW) state with the onset of a superconducting (SC) dome under pressure [22–26]. The signatures of quantum criticality have been chiefly revealed by the observation of linear-T resistivity [27], whose strength scales with the distance from the quantum critical point (QCP) along the pressure axis. Among other fingerprints of quantum criticality, linear resistivity was also found to scale with the amplitude of SDW fluctuations seen by NMR and with the size of the critical temperature T_c for superconductivity [25,28–30].

The contributions of the renormalization-group (RG) approach to the understanding of these quantum critical features were the purpose of several works in the past [31–33]. In the framework of the quasi-1D electron-gas model, for instance, that is how the characteristic sequence of instability lines and the scaling of spin fluctuations with the size of T_c could be fairly well simulated when the antinesting amplitude of the quasi-1D electron band structure was used as a tuning parameter for the QCP [33–35].

More recently, the RG calculations for the umklapp vertex were shown to serve as an input to the linearized Boltzmann theory of electrical transport [36]. From this combination of techniques, first proposed by Buhmann *et al.* [9] in the context of the two-dimensional (2D) Hubbard model for the cuprates, the metallic resistivity across the QCP could be calculated along the pressure (antinesting) axis, and the results could be congruently compared with experiments in the Bechgaard salts [27].

In this work we further exploit the RG-Boltzmann approach and derive the Seebeck coefficient for correlated quasi-1D metals. The numerical integration of the linearized Boltzmann equation when fed in by the RG umklapp vertex function allows a microscopic determination of the energy variation of the anisotropic electron-electron scattering time across the Fermi surface. This variation is mostly influenced by SDW fluctuations and is anisotropic on the Fermi surface. It introduces deviations with respect to a positive and linear-T Seebeck coefficient obtained in the band limit for hole carriers in materials like the Bechgaard salts. The deviations take the form of enhancements that can be not only positive but also negative or electronlike in character. The latter can lead to the sign reversal of the Seebeck coefficient, especially in the neighborhood of the QCP where the interplay between SDW and SC, together with the amplitude of the SDW fluctuations in the metallic state, is the strongest. These results offer an interesting avenue of understanding for the sign reversal of the Seebeck coefficient occurring in the Bechgaard salts near their QCP.

The theory is broadened to systems with stronger umklapp scattering that favors a Mott instability in the 1D portion of their metallic state and which can be approached by the weak-coupling RG from the high-temperature domain. The results are compared to the measurements of the Seebeck coefficient for prototype members of the sulfur-based compounds, the $(\mathrm{TMTTF})_2X$, known as the Fabre salts series [37].

---

*maryam.shahbazi@usherbrooke.ca
†claude.bourbonnais@usherbrooke.ca

2469-9950/2016/94(19)/195153(12)

These compounds are characterized by a more pronounced dimerization of the organic stacks which magnifies umklapp scattering and favors a crossover toward a 1D Mott insulating state.

In Sec. II, we use the linearized Boltzmann theory to derive the expression of the Seebeck coefficient for a quasi-1D three-quarter-filled hole band of a lattice of weakly dimerized chains. In Sec. III, the momentum-resolved renormalized umklapp vertex entering the Boltzmann equation is computed by the RG in the conditions of the quasi-1D electron-gas model simulating the sequence of instabilities found in the Bechgaard salts. In Sec. IV, we present the temperature variations of the Seebeck coefficient across the quantum critical point of the model and examine their link to the energy profile of the inelastic scattering time. In Sec. V, a comparison of the results is made with available data for (TMTSF)$_2X$ and on a broader basis for the more correlated compounds (TMTTF)$_2X$. We conclude in Sec. VI.

II. LINEARIZED BOLTZMANN THEORY OF THE SEEBECK COEFFICIENT

We consider the semiclassical Boltzmann equation for the variation of the quasiparticle Fermi distribution function f in the presence of collisions and a thermal gradient $\nabla_{\boldsymbol r} T$. In steady-state conditions, it takes the form

$$\left[\frac{\partial f(\boldsymbol k)}{\partial t}\right]_{\rm coll} = e\,\boldsymbol{\mathcal E}\cdot\nabla_{\hbar\boldsymbol k} f - \frac{(E_{\boldsymbol k}-\mu)}{T}\nabla_{\boldsymbol r} T\cdot\nabla_{\hbar\boldsymbol k} f, \tag{1}$$

where $E_{\boldsymbol k}$ is the carrier spectrum, μ is the chemical potential, e is the electron charge, and $\boldsymbol{\mathcal E}$ is the electric field set up by the thermal gradient. The collision integral for an array of N_P chains of length L takes the form

$$\begin{aligned}\left[\frac{\partial f(\boldsymbol k)}{\partial t}\right]_{\rm coll} =& -(LN_P)^{-2}\sum_{\boldsymbol k_2,\boldsymbol k_3,\boldsymbol k_4}\frac{1}{2}|\langle \boldsymbol k,\boldsymbol k_2|g_3|\boldsymbol k_3,\boldsymbol k_4\rangle \\ &- \langle \boldsymbol k,\boldsymbol k_2|g_3|\boldsymbol k_4,\boldsymbol k_3\rangle|^2\frac{2\pi}{\hbar}\delta_{\boldsymbol k+\boldsymbol k_2,\boldsymbol k_3+\boldsymbol k_4\pm \boldsymbol G} \\ &\times \delta\big(E_{\boldsymbol k}+E_{\boldsymbol k_2}-E_{\boldsymbol k_3}-E_{\boldsymbol k_4}\big) \\ &\times \{f(\boldsymbol k)f(\boldsymbol k_2)[1-f(\boldsymbol k_3)][1-f(\boldsymbol k_4)] \\ &- [1-f(\boldsymbol k)][1-f(\boldsymbol k_2)]f(\boldsymbol k_3)f(\boldsymbol k_4)\}. \end{aligned}\tag{2}$$

From Fermi's golden rule, the transition probability per unit of time is related to the matrix element $\langle \boldsymbol k,\boldsymbol k_2|g_3|\boldsymbol k_3,\boldsymbol k_4\rangle$ for longitudinal umklapp processes, where $\boldsymbol G = (4k_F,0)$ is the longitudinal reciprocal lattice wave vector and k_F is the 1D Fermi wave vector.

We proceed to the linearization of the Boltzmann equation by introducing [38]

$$f(\boldsymbol k) = \frac{1}{e^{\beta(E_{\boldsymbol k}-\mu)-\phi_{\boldsymbol k}}+1}, \tag{3}$$

where $\phi_{\boldsymbol k}$ is a normalized deviation to thermal equilibrium and $\beta = 1/k_BT$. In the tight-binding approximation, the hole band spectrum for a linear array of N_P weakly coupled dimerized chains is given by

$$E_{\boldsymbol k} = \sqrt{2(t^2+\delta t^2)+2(t^2-\delta t^2)\cos ka} + \epsilon_\perp(k_\perp), \tag{4}$$

where $t\pm\delta t$ are the transfer integrals within and between the dimers ($\delta t>0$, $\delta t \ll t$). Here a is the lattice spacing along the chains, namely, the distance between dimers. The transverse part of the hole spectrum is given by

$$\epsilon_\perp(k_\perp) = 2t_\perp\cos k_\perp d_\perp + 2t_\perp'\cos 2k_\perp d_\perp, \tag{5}$$

where $t_\perp$ and $t_\perp'$ are the first- and second-nearest-neighbor transfer integrals in the direction perpendicular to the chains.

For small deviations with respect to equilibrium, the Fermi distribution becomes

$$f(\boldsymbol k) \simeq f^0(\boldsymbol k) + f^0(\boldsymbol k)[1-f^0(\boldsymbol k)]\phi_{\boldsymbol k}, \tag{6}$$

where $f^0(\boldsymbol k)$ is the equilibrium distribution at $\phi_{\boldsymbol k}=0$. Inserting (6) in Eqs. (1) and (2) leads to the linearized Boltzmann equation

$$\begin{aligned}\mathcal L\phi_{\boldsymbol k} &= e\beta\mathcal E\cdot\boldsymbol v_{\boldsymbol k} - \beta^2k_B(E_{\boldsymbol k}-\mu)\boldsymbol v_{\boldsymbol k}\cdot\nabla_{\boldsymbol r}T \\ &\equiv \mathcal L\phi^{\mathcal E}_{\boldsymbol k} - \mathcal L\phi^{T}_{\boldsymbol k}.\end{aligned}\tag{7}$$

The collision operator $\mathcal L$ satisfies the integral equation

$$\mathcal L\phi^j_{\boldsymbol k} = \sum_{\boldsymbol k'}\mathcal L_{\boldsymbol k,\boldsymbol k'}\phi^j_{\boldsymbol k'}\quad (j=\mathcal E, T), \tag{8}$$

where the kernel is given by

$$\begin{aligned}\mathcal L_{\boldsymbol k,\boldsymbol k'} =& (LN_P)^{-2}\sum_{\boldsymbol k_2,\boldsymbol k_3,\boldsymbol k_4}\frac{1}{2}|\langle \boldsymbol k,\boldsymbol k_2|g_3|\boldsymbol k_3,\boldsymbol k_4\rangle \\ &- \langle \boldsymbol k,\boldsymbol k_2|g_3|\boldsymbol k_4,\boldsymbol k_3\rangle|^2\frac{2\pi}{\hbar}\delta_{\boldsymbol k+\boldsymbol k_2,\boldsymbol k_3+\boldsymbol k_4\pm \boldsymbol G} \\ &\times \delta\big(E_{\boldsymbol k}+E_{\boldsymbol k_2}-E_{\boldsymbol k_3}-E_{\boldsymbol k_4}\big) \\ &\times \frac{f^0(\boldsymbol k_2)[1-f^0(\boldsymbol k_3)][1-f^0(\boldsymbol k_4)]}{[1-f^0(\boldsymbol k)]} \\ &\times \big(\delta_{\boldsymbol k,\boldsymbol k'}+\delta_{\boldsymbol k_2,\boldsymbol k'}-\delta_{\boldsymbol k_3,\boldsymbol k'}-\delta_{\boldsymbol k_4,\boldsymbol k'}\big) \\ =& \sum_{i=1}^{4}\mathcal L^{[i]}_{\boldsymbol k,\boldsymbol k'},\end{aligned}\tag{9}$$

which can be written as the sum of four contributions. The explicit expressions for the diagonal ($\mathcal L^{[1]}$) and off-diagonal ($\mathcal L^{[2-4]}$) terms are calculated according to Ref. [36] in the limit of the quasi-1D electron-gas model. Their expressions, given in the Appendix, are generalizations at arbitrary energy distance from the Fermi level.

The electric current density along the chains resulting from a longitudinal thermal gradient ∇_aT and the induced electric field $\mathcal E_a$ in leading order is given by

$$\begin{aligned} j_a &= \frac{2e}{LN_\perp d_\perp}\sum_{\boldsymbol k} v^a_{\boldsymbol k} f(\boldsymbol k) \\ &\simeq \frac{2e}{LN_\perp d_\perp}\sum_{\boldsymbol k} v^a_{\boldsymbol k} f^0(\boldsymbol k)[1-f^0(\boldsymbol k)]\big(\phi^{\mathcal E}_{\boldsymbol k}-\phi^T_{\boldsymbol k}\big),\end{aligned}\tag{10}$$

where $v^a_{\boldsymbol k}$ is the carrier velocity along the a direction. Introducing the normalized deviations $\bar\phi^{\mathcal E}_{\boldsymbol k} = \phi^{\mathcal E}_{\boldsymbol k}/(e\beta v^a_{k_F}\mathcal E_a)$ and $\bar\phi^{T}_{\boldsymbol k} = \phi^{T}_{\boldsymbol k}/[\beta^2k_Bv^a_{k_F}(E_{\boldsymbol k}-\mu)\nabla_aT]$, which have units of time, this expression can be recast in the form

$$j_a = K_{11}\mathcal E_a - K_{12}\nabla_aT. \tag{11}$$

In the absence of charge current ($j_a = 0$), this leads to the expression of longitudinal Seebeck coefficient Q_a as the ratio

$$Q_a = \frac{\mathcal{E}_a}{\nabla_a T} = \frac{K_{12}}{K_{11}}. \tag{12}$$

Since the product $f^0[1 - f^0]$ is strongly peaked at the Fermi level $E_{\boldsymbol{k}} - \mu \equiv E = 0$, a Sommerfeld expansion of the matrix elements K_{11} and K_{12} yields the following expression for the Seebeck coefficient:

$$\begin{aligned} Q_a = \frac{\pi^3}{3}\frac{k_B^2 T}{|e|}\Bigg\{&\left[-\frac{d\ln\langle N(E,k_\perp)\rangle_{k_\perp}}{dE} - 2\frac{d\ln\langle v^a_{E,k_\perp}\rangle_{k_\perp}}{dE}\right] \\ &- \frac{\partial \ln\langle\bar{\phi}_{E,k_\perp}\rangle_{k_\perp}}{\partial E}\Bigg\}_{E=0} \\ = Q_a^0 + Q_a^c&, \end{aligned} \tag{13}$$

which can be separated into two contributions. The first, denoted Q_a^0, is the sum of the two terms in brackets, which corresponds to the band contribution. It is linked to the energy derivatives of the density of states per spin $\langle N(E,k_\perp)\rangle_{k_\perp}$ $(= \pi^{-1}\langle|\partial k/\partial E_{\boldsymbol{k}}|\rangle_{k_\perp})$, and of the longitudinal velocity $\langle v^a_{E,k_\perp}\rangle_{k_\perp}$ $(= \hbar^{-1}\langle\partial E_{\boldsymbol{k}}/\partial k\rangle_{k_\perp})$. Both quantities are averaged over the Fermi surface for a filling of one hole per dimer ($\langle\cdots\rangle_{k_\perp} = N_P^{-1}\sum_{k_\perp}\cdots$). The second contribution, Q_a^c, is associated with collisions; it is proportional to the energy derivative $\langle\bar{\phi}'_{E=0,k_\perp}\rangle_{k_\perp}$ averaged over the Fermi surface for the normalized deviations $\bar{\phi}^{\mathcal{E}} = \bar{\phi}^T \equiv \bar{\phi}$, namely, the scattering time. The latter obeys the single integral equation

$$\mathcal{L}\bar{\phi}_{\boldsymbol{k}} = \sum_{i,\boldsymbol{k}'}\mathcal{L}^{[i]}_{\boldsymbol{k},\boldsymbol{k}'}\bar{\phi}_{\boldsymbol{k}'} = 1, \tag{14}$$

whose explicit expression is given in (A6). Here $\bar{\phi}_{\boldsymbol{k}} \to \bar{\phi}_{E,k_\perp}$ can be expressed as a function of the energy distance from the Fermi surface and the angle parametrized by $k_\perp$. Expression (13) is reminiscent of the Mott formula for the Seebeck coefficient [21,39]. It should be stressed, however, that the scattering term results from the solution of the $\boldsymbol{k}$-dependent integral equation (14), which goes beyond the relaxation-time approximation used for the Mott result [40].

III. RENORMALIZED UMKLAPP VERTEX

A. The quasi-one-dimensional electron-gas model

The temperature variation of the momentum-dependent umklapp vertex part entering the collision operator of the Boltzmann equation (9) is calculated using the renormalization-group technique in the framework of the quasi-one-dimensional electron-gas model. In the model the longitudinal part of the lattice model for the hole spectrum $E_{\boldsymbol{k}}$ in (4) is linearized with respect to the 1D Fermi points $\pm k_F$. This gives

$$E_{\boldsymbol{k}} - \mu \approx \epsilon^p_{\boldsymbol{k}} = -\hbar v_F(pk - k_F) + \epsilon(k_\perp), \tag{15}$$

where $p = \pm$ refers to right- and left-moving carriers along the chains and $v_F = (t^2 - \delta t^2)a/(\hbar\sqrt{2t^2 + 2\delta t^2})$ is the longitudinal Fermi velocity. According to band calculations, the hopping integrals will be fixed at $t/k_B = 2700$ K and $t_\perp/k_B = 200$ K as typical figures for hopping integrals in compounds like the Bechgaard salts. A second harmonic is added to the transverse tight-binding spectrum which acts as an antinesting tuning parameter $t'_\perp \ll t_\perp$. Antinesting is considered the main parameter simulating the pressure in the model.

Particles interact through three coupling constants defined on the warped Fermi surface sheets $\boldsymbol{k}^p_F(k_\perp) = (k^p_F(k_\perp),k_\perp)$, as parametrized by $k_\perp$ from the condition $\epsilon^p(\boldsymbol{k}^p_F) = 0$ (see the top panel in Fig. 4 below). These are the backward- and forward-scattering amplitudes $g_1(\boldsymbol{k}^-_{F,1},\boldsymbol{k}^+_{F,2};\boldsymbol{k}^-_{F,3},\boldsymbol{k}^+_{F,4})$ and $g_2(\boldsymbol{k}^+_{F,1},\boldsymbol{k}^-_{F,2};\boldsymbol{k}^-_{F,3},\boldsymbol{k}^+_{F,4})$ and the longitudinal umklapp scattering $g_3(\boldsymbol{k}^p_{F,1},\boldsymbol{k}^p_{F,2};\boldsymbol{k}^{-p}_{F,3},\boldsymbol{k}^{-p}_{F,4})$. All couplings are normalized by $\hbar\pi v_F$ and develop from renormalization a momentum dependence on three independent transverse momentum variables.

We will follow previous works [33,34,36] and fix the bare initial repulsive values of the couplings consistently with different experiments and band calculations. Thus for the bare backward scattering, by taking $g_1 \approx 0.32$, one can reasonably account for the observed temperature-dependent enhancement of uniform susceptibility [41]. For the bare longitudinal umklapp term g_3, its bare amplitude is nonzero but very weak, owing to the small dimerization of the organic stacks that introduces some half-filled character to the band. This yields $g_3 \approx g_1(2\delta t/t)$ as a result of the modulation δt of longitudinal hopping integrals responsible for the dimerization gap [42,43]. According to band calculations at low pressure [44], $\delta t/t \approx 0.05,\ldots,0.1$, suggesting we take $g_3 \approx 0.025$ in the following calculations. From these figures, the amplitude of the bare forward scattering can be finally adjusted to the value $g_2 \approx 0.64$ in order to get from the low-$t'_\perp$ RG calculations (see Fig. 1) the right order of magnitude for the observed SDW scale, namely, $T_{\rm SDW} \sim 10$ K for $({\rm TMTSF})_2X$ at ambient pressure [22]. As a function of $t'_\perp$, the application of the RG generates a phase diagram compatible with the

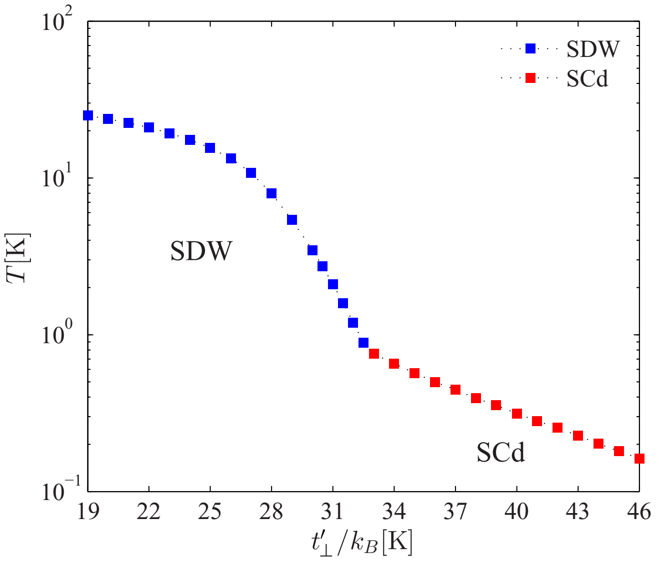

FIG. 1. Renormalization-group results for the phase diagram of the quasi-1D electron-gas model as a function of the antinesting tuning parameter $t'_\perp$ and for the model parameters specified in Sec. III A.

experimental situation [22,27]. There is nothing special in the above choice. Actually, at small umklapp, there exists a whole range of reasonable coupling parameters that would yield a phase diagram comparable to Fig. 1 and then results similar to those for the Seebeck coefficient.

As will discussed in more detail in Sec. V A, one can extend the analysis to the more correlated sulfur-based Fabre salt series (TMTTF)$_2X$ characterized by smaller band parameters and stronger umklapp scattering owing to a larger dimerization of the organic stacks.

B. Renormalization-group results

The RG approach to the above quasi-1D electron-gas model has been described in detail in previous works [32–36]. In essence, it consists of the segmentation of infinitesimal energy shells on either side of the Fermi sheets into N_P patches, whose internal transverse momentum integration in the loop calculations leads to as many $k_\perp$ values. Successive integrations of electronic degrees of freedom on these shells from the (Fermi) energy cutoff $E_F/k_B[=\pi t/(2k_B\sqrt{2})]\equiv$ 3000 K down to zero at the Fermi surface result in the flow of the coupling constants toward their momentum-dependent values as a function of temperature. This is carried out until a singularity is reached in the coupling constants which signals an instability of the electron gas against the formation of a broken-symmetry state at a given temperature.

For the repulsive sector with these (TMTSF)$_2X$ model parameters, this can occur in either a SDW or d-wave SC (SCd) channel depending on the amplitude of antinesting $t'_\perp$. The characteristic sequence of instabilities obtained for $N_P=60$ patches is reviewed in Fig. 1 [36]. At relatively low nesting deviations the magnetic scale $T_{\rm SDW}$ dominates; it drops with $t'_\perp$ down to the critical value $t'^*_\perp$, where instead of a plain quantum critical behavior for antiferromagnetism for which $T_{\rm SDW}$ would reach zero, the ending of $T_{\rm SDW}$ gives rise to an SCd instability at its maximum T_c. The latter then steadily falls off with further increasing $t'_\perp$.

The normal phase we are interested in for the Seebeck coefficient is characterized by spin fluctuations. This is, of course, found in the SDW sector of the phase diagram where the SDW susceptibility $\chi_{\rm SDW}(\boldsymbol{q}_0)$ at the best nesting wave vector of $\epsilon^p_{\boldsymbol{k}}$ at $\boldsymbol{q}_0=(2k_F,\pi/d_\perp)$ develops a singularity at $T_{\rm SDW}$. In the SCd sector, an enhancement, although nonsingular, is still present. It takes the form of a Curie-Weiss temperature profile $\chi_{\rm SDW}\sim(T+\Theta)^{-1}$ over a large temperature domain above T_c ($\Theta\geqslant 0$). The enhancement is quantum critical at $t'^*_\perp$ ($\Theta=0$) and then decays with the decrease of T_c and the rise of the Curie-Weiss scale Θ along the antinesting axis [33].

These short-range SDW correlations of the metallic phase are directly related to the enhancement of umklapp scattering entering the collision operator of the Boltzmann equation. In Fig. 2, we show the temperature and momentum dependence of g_3 on the Fermi surface, as projected in the $(k_{\perp 1},k_{\perp 3})$ plane when $k_{\perp 1}=-k_{\perp 2}$ and $k_{\perp 3}=-k_{\perp 4}$. On the SDW side, the top panel of Fig. 2(a) refers to the high-temperature range ($T>t_\perp$), which shows no structure in the transverse momentum plane for g_3, indicating that SDW correlations are essentially 1D in character and confined along chains. As temperature is lowered below $t_\perp$, transverse short-range order starts to develop, as shown by more intense scattering along the lines $k_{\perp 1}=k_{\perp 3}\pm\pi$ ($d_\perp=1$). This is in accordance with the transverse momentum transfer associated with the best nesting wave vector $\boldsymbol{q}_0$ of the spectrum (15). When the lowest temperature is reached, peaks of stronger intensity appear on the corners at $k_{\perp 1,3}=0,\pm\pi$ and at the best nesting points $\pm\pi/4,\pm 3\pi/4$ of the spectrum (15). These refer to warmer regions of scattering on the Fermi surface at the approach of the critical domain of the SDW instability.

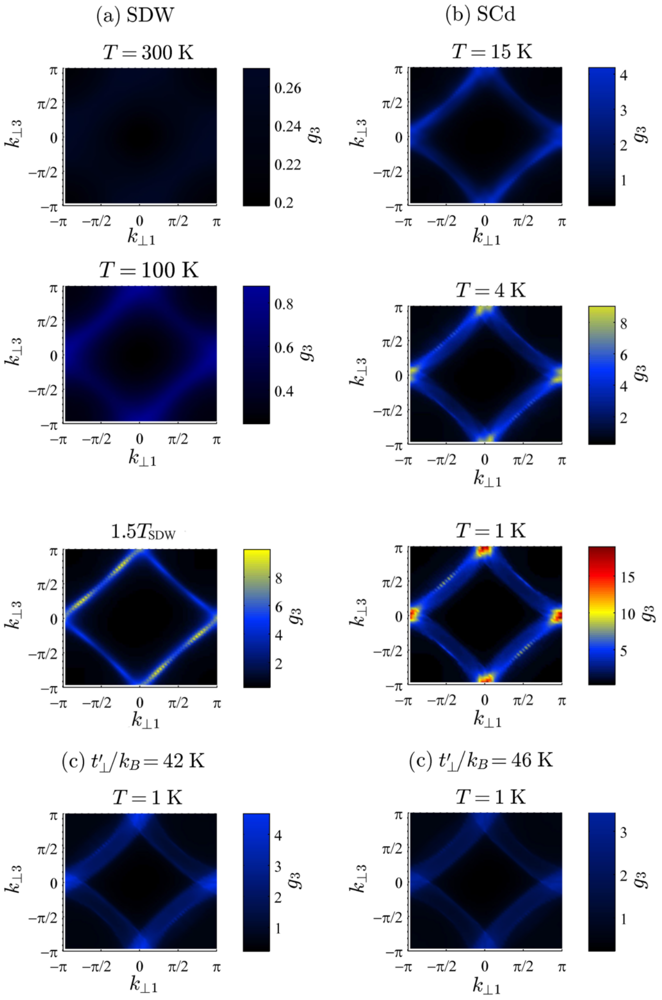

FIG. 2. Renormalized umklapp scattering amplitude $g_3(k_{\perp 1},-k_{\perp 1};k_{\perp 3},-k_{\perp 3})$, projected in the $(k_{\perp 1},k_{\perp 3})$ plane at different temperatures for the metallic phase model parameters specified in Sec. III A. (a) SDW, $t'_\perp/k_B=25$ K ($<t'^*_\perp/k_B$), (b) SCd, $t'_\perp/k_B=$ 35 K ($>t'^*_\perp/k_B$), and (c) SCd, $t'_\perp/k_B=42$ and 46 K at $T=1$ K.

On the SCd side of the phase diagram, in Fig. 2(b), we see a pronounced but nonsingular anisotropic increase of umklapp scattering; peaks are confined around $k_{\perp 1,3}=0,\pm\pi$ on the Fermi surface, where enhanced scattering is found as the temperature is lowered. This enhancement occurs despite the flow of coupling constants towards a SCd fixed point indicative of positive interference between both instabilities. This increase goes hand in hand with the one of SDW correlations in this temperature region, which are directly involved in the mechanism of d-wave Cooper pairing [45–47]. By increasing $t'_\perp$ further, although the same anisotropy of

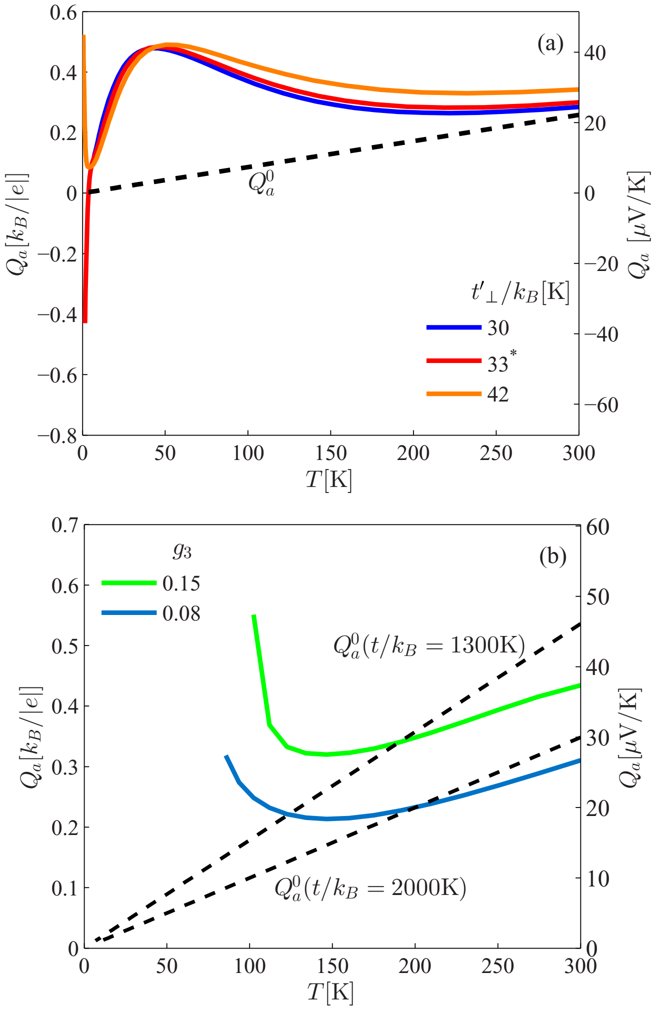

FIG. 3. The longitudinal Seebeck coefficient as a function of temperature for (a) different values of antinesting $t'_\perp$ in the metallic phase and (b) model parameters in the more correlated case with stronger umklapp scattering and lower amplitudes of hopping integrals [$t'_\perp/k_B = 15$ K, $t_\perp/k_B = 100$ K; see Sec. V A on $(\text{TMTTF})_2X$ salts]. The dashed lines gives the band contribution Q_a^0 of Eq. (13) for constant relaxation time in energy.

umklapp enhancement persists, its amplitude scales down with the reduction of T_c, as displayed in Fig. 2(c).

The consequence of this anisotropic growth of umklapp scattering on the temperature dependence of the Seebeck coefficient will be analyzed next.

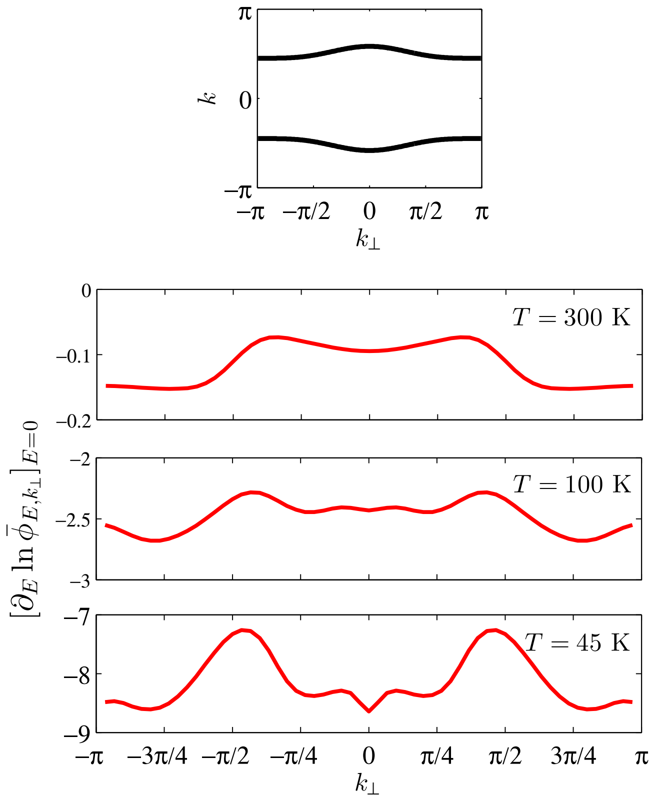

FIG. 4. Open Fermi surface of the quasi-1D electron-gas model (top) and typical variations of the scattering time along the Fermi surface for different high temperatures ($t'_\perp = t'^*_\perp$; bottom).

IV. NUMERICAL RESULTS FOR THE SEEBECK COEFFICIENT

A. High-temperature domain

The temperature dependence of the Seebeck coefficient (13), as obtained from the numerical solution of (A6) for the $(\text{TMTSF})_2X$ model parameters, is shown in Fig. 3(a) in the whole temperature interval of interest. By comparing the amplitude of the two contributions to the Seebeck coefficient in (13), we observe that apart from the high-1D-temperature region, the amplitude of the last term related to scattering dominates the band contribution Q_a^0 [dashed line in Fig. 3(a)] over most of the temperature interval. This gives rise to a shallow minimum for the Seebeck coefficient below which the normalized energy derivative $\bar{\phi}'_{E=0,k_\perp}/\bar{\phi}_{E=0,k_\perp}$ of the normalized scattering time on the Fermi surface grows in importance, as indicated in the lower panels of Fig. 4. The derivative is negative, and according to (13), it gives a positive Q_a^c, as normally expected for hole carriers whose velocity and scattering time decrease with increasing energy.

By lowering the temperature the scattering time derivative gains in amplitude and develops, like g_3 in Fig. 2, anisotropy over the Fermi surface with maximums at $k_\perp = 0, \pm\pi$ and $\pm\pi/4, \pm 3\pi/4$. This leads to a smooth increase of the Seebeck coefficient that levels off at a maximum value around the antinesting $t'_\perp$ scale. This is followed in Fig. 3(a) by a rapid drop at lower temperature which is nearly linear; it evolves toward anomalous features in the amplitude or the sign of the Seebeck coefficient depending on the distance to the critical value $t'^*_\perp$ in the phase diagram. This will be discussed in more detail below.

B. Low-temperature domain and quantum criticality

The results for the Seebeck coefficient in the metallic low-temperature part of the phase diagram are presented in Fig. 5(a) for different values of the antinesting parameter $t'_\perp$. On the SDW side, for $t'_\perp$ relatively well below the critical $t'^*_\perp/k_B$ (=33 K), the decrease of the Seebeck coefficient with lowering

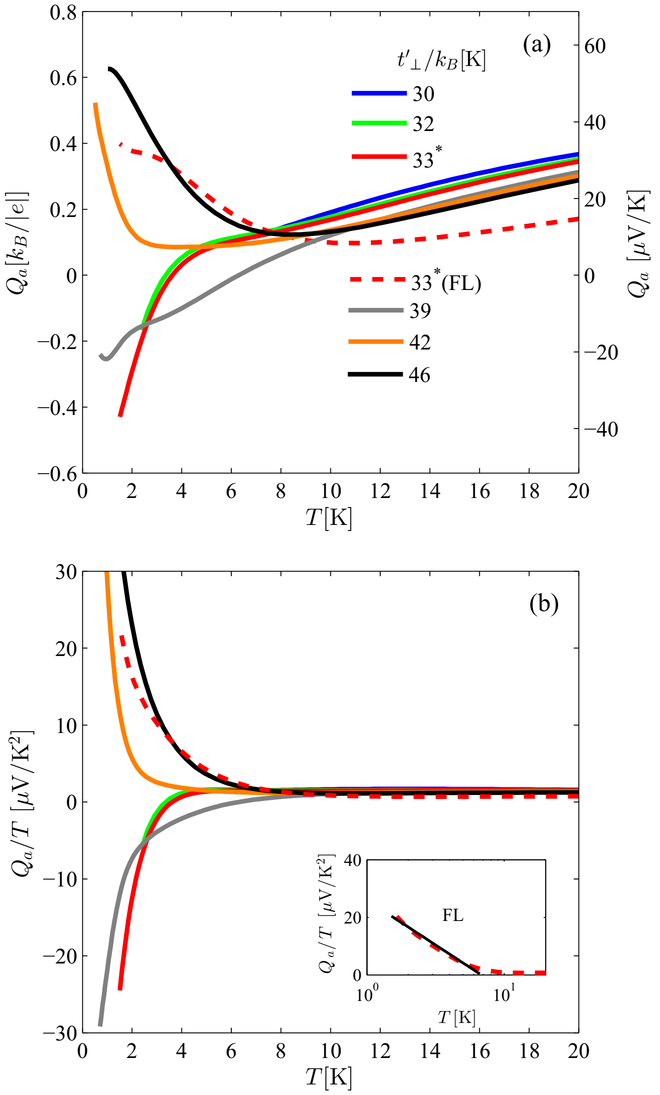

FIG. 5. (a) The longitudinal Seebeck coefficient Q_a and (b) the ratio Q_a/T as a function of T at low temperature and different values of antinesting $t'_\perp$. The value with an asterisk stands for the critical $t'^*_\perp$. The dashed line corresponds to the Fermi liquid limit using a momentum- and temperature-independent g_3 ($= 0.025$) at $t'^*_\perp$. The inset in (b) displays the enhancement on a logarithmic temperature scale. The solid line refers to $Q_a/T \sim \ln T$.

temperature is nearly linear, as indicated by the constant ratio Q_a/T in Fig. 5(b) when the temperature is lowered. Here the slope for Q_a is steeper than for the band contribution Q_a^0 [dashed line in Fig. 3(a)]. The dominant contribution to the Seebeck coefficient comes from Q_a^c, which is positive, resulting from a peak in the energy-dependent quasiparticle scattering time located on the occupied side of the Fermi level at $E < 0$, as shown in the top left panel of Fig. 6(a) above the SDW instability. It is worth noting that in these metallic conditions of the SDW state, the calculated scattering time at the Fermi level ($\sim 10^{-9}$ s) is significantly larger than the one found from the Drude theory of the conductivity of the Bechgaard salts above the SDW state [48] (see the note in Ref. [49]).

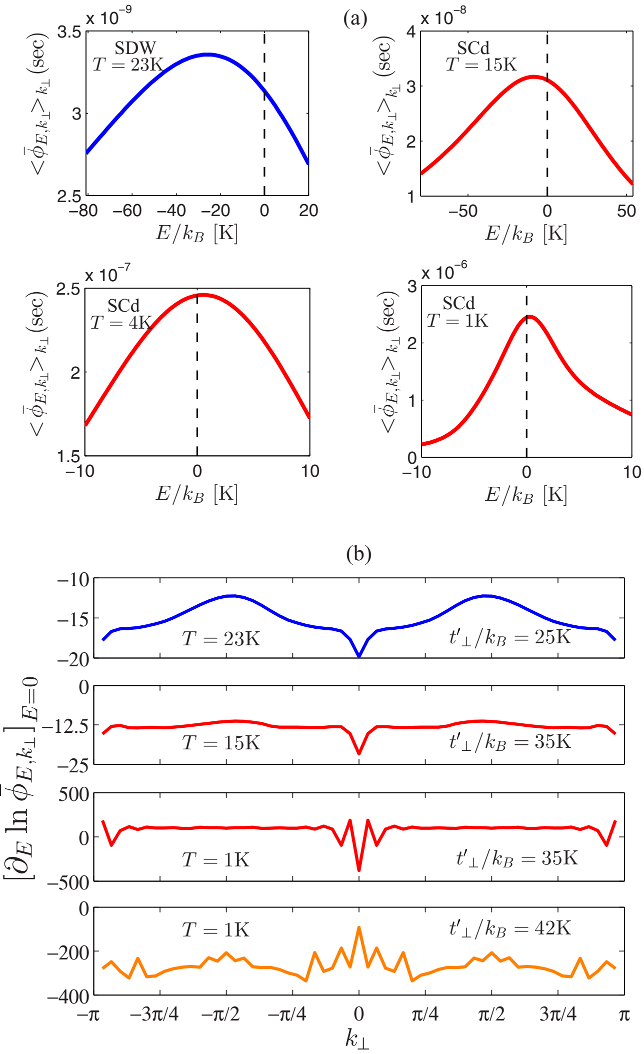

FIG. 6. (a) Variation of the normalized scattering time as a function of energy near the Fermi level at low temperature. Here $t'_\perp/k_B = 25$ and 35 K for the blue and red curves, respectively. (b) The anisotropy of the normalized energy derivative of the scattering time along the Fermi surface at low temperature for different $t'_\perp$.

By raising $t'_\perp$, the temperature scale $T_{\rm SDW}$ in Fig. 1 decays, and at the approach of $t'^*_\perp$ from below, the Seebeck coefficient develops an anomalous enhancement that is opposite in sign. This is depicted by the green lines in Fig. 5. The effect is reinforced when the electron system ultimately enters the SCd domain at $t'^*_\perp$ where T_c is maximum. This indicates that the collision contribution Q_a^c is still negative or electronlike in character and that it exceeds Q_a^0 in amplitude. The sign reversal of the Seebeck coefficient refers to an increase of the scattering time with energy and then to a different asymmetry in the quasiparticle resonance peak of $\langle \bar{\phi}_{E,k_\perp} \rangle$. According to Fig. 6(a), when the temperature is lowered, the latter is shifted from the occupied to the unoccupied side just above the Fermi level at $E > 0$. As for the anisotropy profile of $\bar{\phi}'/\bar{\phi}$ over the Fermi surface, the third panel in Fig. 6(b) reveals that this electronlike component of the Seebeck coefficient comes in large part from the cold regions of scattering, namely, away from the warmer spots centered in $k_\perp = 0$ and $\pm\pi$ in the SCd sector [see Fig. 2(b)]. In the latter regions large oscillations of $\bar{\phi}'/\bar{\phi}$ between positive and negative values tend to average out their contributions to a net positive contribution to the Seebeck coefficient. It is worth noting that the change in sign of the Seebeck coefficient, obtained by tuning $t'_\perp$ across $t'^*_\perp$, occurs in the metallic state, that is, in the absence of any reconstruction of the Fermi surface.

Further above $t'^*_\perp$, the negative enhancement of the Seebeck coefficient weakens and finally transforms into a positive upturn, as shown in Fig. 5. The latter is consistent with a quasiparticle resonance in the scattering time whose peak shifts back below the Fermi level with a negative slope in $\langle \bar{\phi}'_{E=0,k_\perp}\rangle_{k_\perp}$, as shown in the bottom panel in Fig. 6(b). This contributes positively to Q^c_a. At sufficiently large $t'_\perp$, namely, when nesting alterations become large, the g_3 coupling renormalizes less and less with a concomitant weaker anisotropy, as illustrated in Fig. 2(c). In these conditions the Seebeck coefficient should tend to that of a Fermi liquid. This is confirmed when one imposes a momentum- and temperature-independent g_3 in the calculations of the scattering time in (A6), which simulates the conditions of a Fermi liquid. This is shown by the dashed lines in Fig. 5. It is worth noting that the Fermi liquid result for the quasi-1D electron-gas model differs from the linear-T band term Q^0_a. The corresponding ratio Q_a/T in Fig. 5(b) displays a low-temperature variation whose curvature in T slightly exceeds a logarithmic enhancement [inset of Fig. 5(b)]. It is worth pointing out that for a quasi-1D Fermi liquid, the scattering time is energy dependent and goes as $\sim E^2 \ln E$ with logarithmic corrections; it is also asymmetric with respect to the Fermi level due to the presence of antinesting [36,50]. According to Fig. 5(b), the effect of umklapp renormalization leads to enhancements also stronger than logarithmic. Note that previous calculations of fluctuation effects, except this time on the band or thermodynamic contribution Q^0_a, predict logarithmic corrections near a quantum critical point [4].

Following the example of resistivity [36], one can define from $t'^*_\perp$ the zone of influence of quantum criticality where anomalous signs and enhancement of the Seebeck coefficient are found. This is portrayed in Fig. 7. As pointed out previously [31,33,34,36], $t'^*_\perp$ defines a quantum critical point where the entanglement or mutual reinforcement between SDW and SCd instabilities is the strongest, T_c is the highest, and spin fluctuations are quantum critical down to T_c [33]. This is apparently responsible for the electron-type asymmetry in the energy dependence of electron-electron scattering time and therefore for the sign reversal of the Seebeck coefficient.

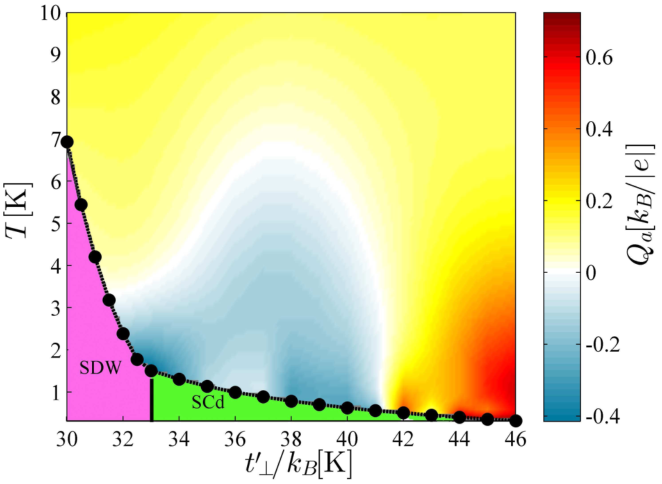

FIG. 7. Amplitude of the Seebeck coefficient at low temperature as a function of antinesting.

The amplitude of reinforcement between SDW and SCd pairings is correlated to the size of T_c. This is reflected in Figs. 2(b) and 2(c) by the anisotropic flow of g_3 responsible for the growth SDW fluctuations, which scales with $t'_\perp$. As discussed in detail in preceding works [33,34,51], this scaling gives rise to an extended region of quantum critical SDW effects in the phase diagram that goes over the edges of an inverted-triangle-shaped domain usually expected when only the SDW state is present and Cooper pairing is absent. According to Fig. 7, extended quantum criticality for the Seebeck coefficient manifests by a domelike domain of negative Q_a, characterized along the $t'_\perp$ axis by a broadened base at low temperature and a top peaking above $t'^*_\perp$ at a sizable T_c [52]. The crossover toward the region of positive Seebeck coefficients is achieved at high enough $t'_\perp$. However, fluctuation effects and deviations from Fermi liquid predictions down to the lowest temperature still persist. It is only at large $t'_\perp$, when T_c is small enough and g_3 renormalizes sufficiently weakly, that the Fermi liquid limit is recovered.

V. COMPARISON WITH EXPERIMENTS IN LOW-DIMENSIONAL ORGANIC CONDUCTORS

We now turn to the comparison of the above results with experiments. In this matter, it is instructive to first examine the Seebeck coefficient for some members of the $(\mathrm{TMTTF})_2X$ series, the so-called Fabre salts, which are known to exhibit a more correlated normal phase than the Bechgaard salts in normal pressure conditions as a result of stronger umklapp scattering [23,53]. The weak-coupling RG can be used to compute the flow of umklapp scattering down to the approach of the Mott strong-coupling region. After this incursion in the physics of the Fabre salts, we then proceed to the discussion of the Seebeck coefficient experiments in the Bechgaard salts in light of the results of the present calculations.

A. The Fabre salts $(\mathrm{TMTTF})_2X$

The Fabre salts, with $X =$ PF_6, AsF_6, Br, . . ., form a series of quasi-1D conductors characterized by the same crystallographic structure as the Bechgaard salt $(\mathrm{TMTSF})_2X$ series [54]. The difference between the two series lies in the chemical composition of the TMTTF organic molecule for which the sulfur atoms are substituted in place of selenium in TMTSF. As a consequence, the amplitude of the dimerization of TMTTF stacks turns out to be more pronounced in the solid state, along with band parameters that are typically smaller than those found in $(\mathrm{TMTSF})_2X$ (see Sec. III) [44,55]. In normal pressure conditions, the $(\mathrm{TMTTF})_2X$ are thus more one-dimensional in character and also more correlated than $(\mathrm{TMTSF})_2X$ through essentially a stronger influence of electronic umklapp processes.

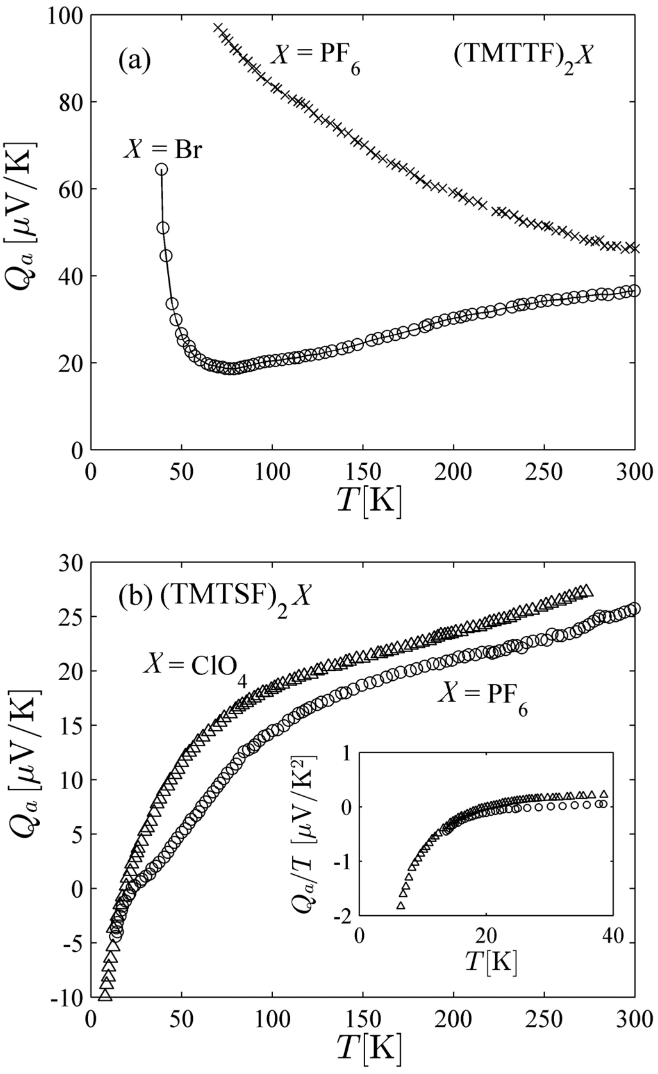

FIG. 8. Temperature dependence of Seebeck coefficients in (a) a few $(\mathrm{TMTTF})_2X$ salts at ambient pressure (after Ref. [37]) and (b) $(\mathrm{TMTSF})_2X$ in the metallic state above T_{SDW}, $X = \mathrm{PF}_6$, and T_c, $X = \mathrm{ClO}_4$. The inset shows the sign reversal of the ratio Q_a/T in the low-temperature domain (after Ref. [15]).

This is exemplified by an upturn in electrical resistivity at the intermediate temperature T_ρ, indicative of strong umklapp scattering that evolves towards an insulating 1D Mott behavior [53,56–58]. Long-range ordered states can be found at much lower temperature, which can involve charge, spin, and even lattice degrees of freedom [23]. A remarkable property of the series emerges when sufficiently high pressure is applied to $(\mathrm{TMTTF})_2X$, which ultimately maps their physical properties to those of $(\mathrm{TMTSF})_2X$ at low pressure.

$(\mathrm{TMTTF})_2\mathrm{PF}_6$ is a prototype compound of the Fabre series characterized by the temperature scale $T_\rho \simeq 220$ K [56,57]. The measurements of the Seebeck coefficient by Mortensen *et al.* [37] for this compound are reproduced in Fig. 8(a). The data show a monotonic increase of the Seebeck coefficient with decreasing temperature. The increase is consistent with nonmetallic behavior shown by resistivity in the same range of temperature [56,57].

The calculated results for a compound like $(\mathrm{TMTTF})_2\mathrm{PF}_6$ are displayed in Fig. 3(b); when in accordance with band calculations [44], smaller hopping terms ($t/k_B = 1300$ K, $t_\perp/k_B = 100$ K, $E_F/k_B = 1500$ K, $t'_\perp/k_B = 15$ K) [59] and larger amplitudes for the bare umklapp ($g_3 = 0.15$) are used. With these figures, the instability at T_{SDW} occurs at much higher temperature ($T_{\mathrm{SDW}} = T_\rho \sim t_\perp$) and corresponds to the 1D Mott scale T_ρ at the one-loop level of the RG [23,53]. The important reduction of the longitudinal hopping t is responsible for a larger amplitude of the Seebeck coefficient, which is mainly dominated by the band term Q_a^0 at high temperature, as shown by the dashed line of Fig. 3(b). Note that this term surpasses the total Q_a, indicating that the contribution of Q_a^c coming from collisions is relatively small but negative at very high temperature. The resulting Q_a then shows a smooth decrease with decreasing temperature, contrary to observation in $(\mathrm{TMTTF})_2\mathrm{PF}_6$. However, the effect of the collision term quickly becomes positive and gives rise to an upturn of the Seebeck coefficient with lowering temperature, as observed.

The case of $(\mathrm{TMTTF})_2\mathrm{Br}$ is also of interest since, along the pressure axis of a generalized phase diagram including both families, this compound is chemically shifted at about half the distance between $(\mathrm{TMTTF})_2\mathrm{PF}_6$ and the members of the $(\mathrm{TMTSF})_2X$ series at low pressure [23]. For normal-state properties, for instance, this is illustrated by the intermediate-scale $T_\rho \simeq 100$ K seen in resistivity [56,60], in line with a smaller dimerization of the organic stacks for $(\mathrm{TMTTF})_2\mathrm{Br}$. The temperature variation of the Seebeck coefficient for the bromine salt is displayed in Fig. 8 [37]. At room temperature the coefficient is smaller in amplitude compared to that of $(\mathrm{TMTTF})_2\mathrm{PF}_6$; it drops as temperature is lowered, consistent with the more pronounced metallic character of this salt in this temperature range. However, the variation is not linear in temperature but reveals an enhancement with respect to the free-carrier situation. A minimum for temperature under T_ρ is reached, followed by an increase that evolves toward a characteristic $1/T$ behavior for Q_a at sufficiently low temperature [37], in agreement with a well-defined insulating (Mott) gap.

By using intermediate figures for the band parameters ($t = 2000$ K, $t_\perp = 100$ K, $E_F = 2200$ K, $t'_\perp/k_B = 15$ K) and bare umklapp amplitude ($g_3 = 0.08$), the amplitude of the calculated Seebeck coefficient at ambient temperature in Fig. 3 is intermediate between $(\mathrm{TMTTF})_2\mathrm{PF}_6$ and $(\mathrm{TMTSF})_2X$, as shown in Figs. 8(a) and 8(b). The calculated decrease of Q_a, although enhanced compared to Q_a^0 due to inelastic scattering, is less rapid than observed. The flow to strong umklapp scattering then results in the upturn in the Seebeck coefficient.

B. The Bechgaard salts $(\mathrm{TMTSF})_2X$

The Seebeck coefficient measured for the $X = \mathrm{PF}_6$ and ClO_4 members of the Bechgaard salts is shown in Fig. 8(b). Let us recall that in contrast to the sulfur-based $(\mathrm{TMTTF})_2X$ compounds at low pressure, T_ρ is an irrelevant 1D scale for $(\mathrm{TMTSF})_2X$ since these materials are metallic down to the temperature of onset of long-range order ($T_{\mathrm{SDW},c} \ll t_\perp$). In this range of temperature the system becomes effectively 2D regarding one-particle coherence, although it is strongly anisotropic. In Fig. 8(b) we reproduce the temperature dependence of Q_a obtained by Chai *et al.* [15] (see also Choi *et al.* [16], Sun *et al.* [17], Chaikin *et al.* [18], and Gubser *et al.* [19]). $(\mathrm{TMTSF})_2\mathrm{PF}_6$ shows SDW ordering at $T_{\mathrm{SDW}} \simeq 12.5$ K, whereas for $(\mathrm{TMTSF})_2\mathrm{ClO}_4$ the anion (ClO_4) ordering in slow-cooling conditions pushes the compound on the SC part of the phase diagram of series with $T_c \simeq 1.2$ K [22,61].

Close to ambient temperature, the Seebeck coefficient for both compounds reveals values relatively close to the calculated band limit Q_a^0 given in Fig. 3 using the $(\mathrm{TMTSF})_2X$ band parameters of Sec. III. At lower temperature a positive enhancement with respect to a T-linear descent is observed for both compounds, in qualitative agreement with the one found in the present calculations in Fig. 3. However, in contrast to predictions, no maximum for Q_a is found experimentally; the data in Fig. 8(b) rather show a shoulderlike structure that precedes the low-temperature descent of the Seebeck coefficient. This suggests that the energy variation of the collision term is less rapid than predicted in this temperature range. We do not exclude, however, that such a maximum would show up if a small pressure was applied to a compound like $(\mathrm{TMTTF})_2\mathrm{Br}$ [see Fig. 8(a)], which would suppress T_ρ [60] and shift the compound on the left-hand side of $(\mathrm{TMTSF})_2X$ along the pressure axis [23] (see also [62]).

For both compounds, Fig. 8(b) shows that the drop seen at low temperature for the Seebeck coefficient does not extrapolate toward zero but exhibits negative enhancement from Q_a^c that evolves toward a net sign reversal of the Seebeck coefficient. Because T_c for $(\mathrm{TMTSF})_2\mathrm{ClO}_4$ is small, this sign reversal can occur down to a very low temperature of the metallic state, as shown in the inset of Fig. 8(b) for the ratio Q_a/T. The sign reversal of the Seebeck coefficient occurs in the metallic state in the absence of a Fermi surface reconstruction that would transform the nature of carriers from hole to electron type. The crossing temperature $T_0 \simeq 18$ K observed for the sign reversal is distinctly larger than calculated in Fig. 7. Although the set of model parameters (hopping integral and interaction strength) could be slightly modified in order to increase T_0 and make the comparison with the data in Fig. 8(b) more favorable quantitatively, it must be stressed, however, that as a crossover temperature, T_0 is found to be appreciably lower in other experiments [14,16–19]. The origin of this disparity in the observed T_0 is not clear, limiting the comparison between theory and experiments to a more qualitative level.

The present calculations can thus provide an avenue of explanation for the sign reversal of the Seebeck coefficient in terms of an anomalous energy dependence of the inelastic umklapp scattering time at the Fermi level which becomes electronlike in character (see Fig. 6). This transformation has its origin in the SDW fluctuations which act as the source of enhancement of umklapp scattering. As we have seen in Sec. III A, the development of these spin fluctuations can be greatly enhanced over sizable intervals of temperature and antinesting in the neighborhood of the quantum critical point $t_\perp'^*$ [see, for example, Fig. 2(b)] [33], in qualitative agreement with the spreading of the sign reversal of the Seebeck coefficient found in Figs. 5 and 7. It is worth stressing that NMR experiments for the temperature variation of the nuclear spin lattice relaxation rate have provided considerable evidence for the presence of spin fluctuations for both compounds in the same temperature range and their smooth decaying amplitude with pressure [25,28,29,41,63,64].

VI. SUMMARY AND CONCLUDING REMARKS

In the work developed above, a derivation of the Seebeck coefficient in quasi-1D interacting electron systems has been carried out from a numerical solution of the linearized Boltzmann equation using the renormalization-group method for the evaluation of the electron-electron scattering matrix element. From a parametrization of the electron-gas model compatible with the spin-density wave to the superconducting sequence of orderings found in organic superconductors under pressure, the temperature variation of the Seebeck coefficient in the metallic phase was calculated. It was shown to develop marked deviations with respect to the hole-band linear-T prediction. These deviations exhibited striking expression in an extended quantum critical region of the metallic phase linked to the juncture of antiferromagnetic and superconducting orders. It is where the enhancement of the Seebeck coefficient undergoes a sign reversal, attributable to an anomalous low-energy variation of the anisotropic electron-electron scattering time becoming electronlike in character over most of the Fermi surface. Spin fluctuations, which act as a source of inelastic umklapp scattering, appear to be a key determinant for this sign reversal, which occurs in the absence of a Fermi surface reconstruction. It is only when the antinesting parameter, which simulates the role of pressure in real materials, is tuned sufficiently far away from the quantum critical point that a Fermi liquid type of enhancement of the Seebeck coefficient is recovered.

The results were shown to capture many features of existing data in quasi-1D conductors like the Bechgaard salts $(\mathrm{TMTSF})_2X$, in particular the crossover to negative values of the Seebeck coefficient at low temperature in the neighborhood of their quantum critical point along the pressure axis. The size of the enhancement with respect to the band prediction is also fairly well taken into account, suggesting that electron-electron scattering in the presence of electron-hole asymmetry mainly due to nesting alterations is likely to be the most important process governing the temperature dependence of the thermoelectric response of these materials. The results of the calculations are obtained at arbitrary antinesting distance from the quantum critical point of the phase diagram, so they can serve as a stimulus for future experiments of the Seebeck coefficient in Bechgaard salts as a function of applied hydrostatic pressure. Such a systematic study is lacking so far. Following the example of previous electrical transport [27,65] and NMR studies [25,28,29,66], it would be worthwhile to check if the Fermi liquid behavior of the Seebeck coefficient is recovered sufficiently far above the quantum critical pressure.

It is also important to confirm from other experimental probes the anomalous particle-hole asymmetry in the inelastic scattering time in systems like the Bechgaard salts. In this respect, the quasiparticle lifetime extracted from the photoemission cross section may be useful to directly probe the anomalous energy profile of inelastic scattering near the Fermi level. Among other possible probes is the Hall effect. The temperature dependence of the Hall coefficient in the normal state may reveal asymmetry in the scattering dynamics, especially in the absence of Fermi surface reconstruction that would affect the carrier concentration. In this respect, it is worth mentioning the anomalous temperature dependence of the Hall coefficient reported for a compound like (TMTSF)$_2$PF$_6$. The coefficient is found to strongly deviate from the band prediction at the approach of T_{SDW} [67].

The present theory of the Seebeck coefficient was also applied to the more correlated Fabre (TMTTF)$_2X$ series, whose members with centrosymmetrical anions X are known to become Mott insulators at relatively high temperature in normal pressure conditions. Stronger umklapp scattering and narrower bands characterize these materials. This precipitates an instability toward an insulating state at much higher temperature and, accordingly, yields a pronounced enhancement of the Seebeck coefficient that is present in experiments.

ACKNOWLEDGMENTS

The authors would like to thank H. Bakrim and A. Sedeki for their valuable comments on computing aspects of this work. C.B. thanks the National Science and Engineering Research Council of Canada (NSERC) under Grant No. RGPIN-2016-06017, and the Réseau Québécois des Matériaux de Pointe (RQMP) for financial support. Simulations were performed on computers provided by Canadian Foundation for Innovation, the Ministère de l'Éducation des Loisirs et du Sport (Québec), Calcul Québec, and Compute Canada.

APPENDIX: LINEARIZED BOLTZMANN EQUATION

In the presence of an external longitudinal thermal gradient and induced electric field, the linearized Boltzmann equation for the normalized deviations $\bar{\phi}_{\boldsymbol{k}}$ $(= \bar{\phi}_{\boldsymbol{k}}^{j=\mathcal{E},T})$ can be put in the single form of Eq. (14):

$$\mathcal{L}\bar{\phi}_{\boldsymbol{k}} = \sum_{i=1}^{4}\sum_{\boldsymbol{k}'}\mathcal{L}^{[i]}_{\boldsymbol{k},\boldsymbol{k}'}\bar{\phi}_{\boldsymbol{k}'} = 1. \tag{A1}$$

The collision operator is expressed as the sum of four terms,

$$\begin{aligned}\sum_{i=1}^{4}\mathcal{L}^{[i]}_{\boldsymbol{k},\boldsymbol{k}'} = {}& \frac{1}{(LN_P)^2}\sum_{\boldsymbol{k}_2,\boldsymbol{k}_3,\boldsymbol{k}_4}\frac{1}{2}|\langle\boldsymbol{k},\boldsymbol{k}_2|g_3|\boldsymbol{k}_3,\boldsymbol{k}_4\rangle - \langle\boldsymbol{k},\boldsymbol{k}_2|g_3|\boldsymbol{k}_4,\boldsymbol{k}_3\rangle|^2\frac{2\pi}{\hbar}\delta_{\boldsymbol{k}+\boldsymbol{k}_2,\boldsymbol{k}_3+\boldsymbol{k}_4+p\boldsymbol{G}}\\ & \times\delta\big(\varepsilon^{p}_{\boldsymbol{k}} + \varepsilon^{p_2}_{\boldsymbol{k}_2} - \varepsilon^{p_3}_{\boldsymbol{k}_3} - \varepsilon^{p_4}_{\boldsymbol{k}_4}\big)\frac{f^0(\boldsymbol{k}_2)[1-f^0(\boldsymbol{k}_3)][1-f^0(\boldsymbol{k}_4)]}{[1-f^0(\boldsymbol{k})]}(\delta_{\boldsymbol{k},\boldsymbol{k}'} + \delta_{\boldsymbol{k}_2,\boldsymbol{k}'} - \delta_{\boldsymbol{k}_3,\boldsymbol{k}'} - \delta_{\boldsymbol{k}_4,\boldsymbol{k}'}).\end{aligned} \tag{A2}$$

The amplitude of the umklapp vertex is evaluated by the RG in the framework of the quasi-1D electron-gas model,

$$\begin{aligned}\langle\boldsymbol{k}_1,\boldsymbol{k}_2|g_3|\boldsymbol{k}_3,\boldsymbol{k}_4\rangle &= \pi\hbar v_F g_3\big(\boldsymbol{k}^{p}_{F,1},\boldsymbol{k}^{p}_{F,2};\boldsymbol{k}^{-p}_{F,3},\boldsymbol{k}^{-p}_{F,4}\big)\\ &= \pi\hbar v_F g_3(k_{\perp 1},k_{\perp 2};k_{\perp 3},k_{\perp 4}),\end{aligned} \tag{A3}$$

where the position on the Fermi surface is parametrized by the transverse wave vectors. To solve the equation with the explicit form of matrix elements shown in Eq. (A2), we separate the momentum conservation constraint into longitudinal and transverse components [50],

$$\delta_{\boldsymbol{k}+\boldsymbol{k}_2,\boldsymbol{k}_3+\boldsymbol{k}_4+p\boldsymbol{G}} = \delta_{k_\perp+k_{\perp 2},k_{\perp 3}+k_{\perp 4}}\frac{2\pi}{L}\hbar v_F\delta\big(\varepsilon^{p}_{\boldsymbol{k}} + \varepsilon^{p_2}_{\boldsymbol{k}_2} + \varepsilon^{p_3}_{\boldsymbol{k}_3} + \varepsilon^{p_4}_{\boldsymbol{k}_4} - \Sigma\big), \tag{A4}$$

where $\Sigma = \epsilon_\perp(k_\perp) + \epsilon_\perp(k_{\perp 2}) + \epsilon_\perp(k_{\perp 3}) + \epsilon_\perp(k_{\perp 4})$. The summation over the momentum vectors can be written as

$$\frac{1}{LN_P}\sum_{\boldsymbol{k}} = \sum_{p}\int\frac{d\varepsilon^{p}_{\boldsymbol{k}}}{2\pi\hbar v_F}\frac{1}{N_P}\sum_{k_\perp}. \tag{A5}$$

Carrying out the integration over $\varepsilon^{p'}_{\boldsymbol{k}'}$ and rearranging the terms, we arrive at the final equation,

$$\begin{aligned}\frac{\pi}{\beta\hbar}\frac{1}{N_P^2}\sum_{k'_\perp,k_{\perp 3},k_{\perp 4}}\Bigg\{ & |g_3(k_\perp,k_{\perp 3}+k_{\perp 4}-k_\perp;k_{\perp 3},k_{\perp 4}) - g_3(k_\perp,k_{\perp 3}+k_{\perp 4}-k_\perp;k_{\perp 4},k_{\perp 3})|^2\delta_{k_\perp,k'_\perp}\\ & \times\frac{\beta\Sigma'/4\cosh(\beta E/2)}{\cosh[\beta(\Sigma'/4-E/2)]\sinh(\beta\Sigma'/4)} + |g_3(k_\perp,k'_\perp;k_{\perp 3},k_{\perp 4}) - g_3(k_\perp,k'_\perp;k_{\perp 4},k_{\perp 3})|^2\\ & \times\frac{\beta\Sigma''/4\cosh(\beta E/2)}{\cosh[\beta(\Sigma''/4-E/2)]\sinh(\beta\Sigma''/4)}\delta_{k_\perp+k'_\perp,k_{\perp 3}+k_{\perp 4}} - 2|g_3(k_\perp,k_{\perp 3};k'_\perp,k_{\perp 4}) - g_3(k_\perp,k_{\perp 3};k_{\perp 4},k'_\perp)|^2\\ & \times\frac{\beta\Sigma''/4\cosh(\beta E/2)}{\cosh[\beta(\Sigma''/4-E/2)]\sinh(\beta\Sigma''/4)}\delta_{k_\perp+k_{\perp 3},k'_\perp+k_{\perp 4}}\Bigg\}\bar{\phi}_{E,k'_\perp} = 1,\end{aligned} \tag{A6}$$

where $\Sigma' = \epsilon_\perp(k_\perp) + \epsilon_\perp(k_{\perp 3}+k_{\perp 4}-k_\perp) + \epsilon_\perp(k_{\perp 3}) + \epsilon_\perp(k_{\perp 4})$ and $\Sigma'' = \epsilon_\perp(k_\perp) + \epsilon_\perp(k'_\perp) + \epsilon_\perp(k_{\perp 3}) + \epsilon_\perp(k_{\perp 4})$. By inserting the RG results of Sec. III A for the momentum-resolved umklapp scattering, the numerical solution of (A6) for $\bar{\phi}_{E,k_\perp}$ allows the evaluation of the scattering contribution Q^c_a to the Seebeck coefficient (13).

[1] S. Hartmann, N. Oeschler, C. Krellner, C. Geibel, S. Paschen, and F. Steglich, Phys. Rev. Lett. **104**, 096401 (2010).
[2] H. Pfau, R. Daou, M. Brando, and F. Steglich, Phys. Rev. B **85**, 035127 (2012).
[3] Z. Ren, G. W. Scheerer, G. Lapertot, and D. Jaccard, Phys. Rev. B **94**, 024522 (2016).
[4] I. Paul and G. Kotliar, Phys. Rev. B **64**, 184414 (2001).
[5] K.-S. Kim and C. Pépin, Phys. Rev. B **81**, 205108 (2010).
[6] S. Arsenijević, H. Hodovanets, R. Gaál, L. Forró, S. L. Bud'ko, and P. C. Canfield, Phys. Rev. B **87**, 224508 (2013).
[7] F. Laliberté, J. Chang, N. Doiron-Leyraud, E. Hassinger, R. Daou, M. Rondeau, B. J. Ramshaw, R. Liang, D. A. Bonn, W. N. Hardy, S. Pyon, T. Takayama, H. Takagi, I. Sheikin, L. Malone, C. Proust, K. Behnia, and L. Taillefer, Nat. Commun. **2**, 432 (2011).
[8] R. Daou, N. Doiron-Leyraud, D. LeBoeuf, S. Y. Li, F. Laliberté, O. Cyr-Choinière, Y. J. Jo, L. Balicas, J.-Q. Tan, J.-S. Zhou, J. B. Goodenough, and L. Taillefer, Nat. Phys. **5**, 31 (2009).
[9] J. M. Buhmann, M. Ossadnik, T. M. Rice, and M. Sigrist, Phys. Rev. B **87**, 035129 (2013).
[10] L.-F. Arsenault, B. S. Shastry, P. Sémon, and A.-M. S. Tremblay, Phys. Rev. B **87**, 035126 (2013).
[11] P. Li, K. Behnia, and R. L. Greene, Phys. Rev. B **75**, 020506 (2007).
[12] F. Gollnik and M. Naito, Phys. Rev. B **58**, 11734 (1998).
[13] K. Bechgaard, C. Jacobsen, K. Mortensen, H. Pedersen, and N. Thorup, Solid State Commun. **33**, 1119 (1980).
[14] K. Mortensen, Solid State Commun. **44**, 643 (1982).
[15] Y. Chai, H. Yang, J. L. C. Sun, H. Gao, X. Chen, L. Cao, and J.-C. Lasjaunias, J. Phys. Soc. Jpn. **78**, 063602 (2009).
[16] E. S. Choi, H. Y. Kang, Y. J. Jo, J. Yeom, and W. Kang, Synth. Met. **120**, 1069 (2002).
[17] C.-H. Sun, H.-S. Yang, J. Liu, H.-X. Gao, J.-B. Wang, L. Cheng, L.-Z. Cao, and J. C. Lasjaunias, J. Phys. Condens. Matter **20**, 235223 (2008).
[18] P. M. Chaikin, M.-Y. Choi, and R. L. Greene, J. Phys. Colloq. **44**, C3783 (1983).
[19] D. U. Gubser, W. W. Fuller, T. O. Poehler, J. Stokes, D. O. Cowan, M. Lee, and A. N. Bloch, Mol. Cryst. Liq. Cryst. **79**, 225 (1982).
[20] Y. Machida, X. Lin, W. Kang, K. Izawa, and K. Behnia, Phys. Rev. Lett. **116**, 087003 (2016).
[21] K. Behnia, *Fundamentals of Thermoelectricity* (Oxford University Press, Oxford, 2015).
[22] D. Jérome and H. J. Schulz, Adv. Phys. **31**, 299 (1982).
[23] C. Bourbonnais and D. Jérome, in *The Physics of Organic Superconductors and Conductors*, edited by A. Lebed, Springer Series in Materials Science Vol. 110 (Springer, Heidelberg, 2008), p. 357.
[24] L. Taillefer, Annu. Rev. Condens. Matter Phys. **1**, 51 (2010).
[25] S. E. Brown, Physica C (Amsterdam, Neth.) **514**, 279 (2015).
[26] D. Jérome and S. Yonezawa, C. R. Phys. **17**, 357 (2016).
[27] N. Doiron-Leyraud, P. Auban-Senzier, S. René de Cotret, C. Bourbonnais, D. Jérome, K. Bechgaard, and L. Taillefer, Phys. Rev. B **80**, 214531 (2009).
[28] S. E. Brown, P. M. Chaikin, and M. J. Naughton, in *The Physics of Organic Superconductors and Conductors*, edited by A. Lebed, Springer Series in Materials Science Vol. 110 (Springer, Heidelberg, 2008), p. 49.
[29] F. Creuzet, C. Bourbonnais, L. G. Caron, D. Jérome, and A. Moradpour, Synth. Met. **19**, 277 (1987).
[30] Y. Kimura, M. Misawa, and A. Kawamoto, Phys. Rev. B **84**, 045123 (2011).
[31] R. Duprat and C. Bourbonnais, Eur. Phys. J. B **21**, 219 (2001).
[32] J. C. Nickel, R. Duprat, C. Bourbonnais, and N. Dupuis, Phys. Rev. B **73**, 165126 (2006).
[33] C. Bourbonnais and A. Sedeki, Phys. Rev. B **80**, 085105 (2009).
[34] A. Sedeki, D. Bergeron, and C. Bourbonnais, Phys. Rev. B **85**, 165129 (2012).
[35] Y. Fuseya, C. Bourbonnais, and K. Miyake, Europhys. Lett. **100**, 5708 (2012).
[36] M. Shahbazi and C. Bourbonnais, Phys. Rev. B **92**, 195141 (2015).
[37] K. Mortensen, E. M. Conwell, and J. M. Fabre, Phys. Rev. B **28**, 5856 (1983).
[38] H. Haug and A. P. Jauho, in *Quantum Kinetics in Transport and Optics of Semiconductors*, edited by M. Cardona and P. Fulde, Springer Series in Solid-State Sciences Vol. 110 (Springer, Heidelberg, 2008), p. 3.
[39] M. Cutler and N. F. Mott, Phys. Rev. **181**, 1336 (1969).
[40] J. M. Ziman, *Principles of the Theory of Solids* (Cambridge University Press, London, 1972).
[41] P. Wzietek, F. Creuzet, C. Bourbonnais, D. Jérome, K. Bechgaard, and P. Batail, J. Phys. I **3**, 171 (1993).
[42] S. Barisic and S. Brazovskii, in *Recent Developments in Condensed Matter Physics*, edited by J. T. Devreese (Plenum, New York, 1981), Vol. 1, p. 327.
[43] K. Penc and F. Mila, Phys. Rev. B **50**, 11429 (1994).
[44] L. Ducasse, A. Abderrabba, J. Hoarau, M. Pesquer, B. Gallois, and J. Gaultier, J. Phys. C **19**, 3805 (1986).
[45] M. T. Béal-Monod, C. Bourbonnais, and V. J. Emery, Phys. Rev. B **34**, 7716 (1986).
[46] L. G. Caron and C. Bourbonnais, Physica B+C (Amsterdam) **143**, 453 (1986).
[47] V. J. Emery, Synth. Met. **13**, 21 (1986).
[48] M. Dressel, A. Schwartz, G. Gruner, and L. Degiorgi, Phys. Rev. Lett. **77**, 398 (1996).
[49] This much longer time scale for scattering processes would be rather compatible with the so-called zero-frequency mode seen in optical conductivity of the Bechgaard salts in their low-temperature metallic state [48].
[50] L. P. Gorkov and M. Mochena, Phys. Rev. B **57**, 6204 (1998).
[51] C. Bourbonnais and A. Sedeki, C. R. Phys. **12**, 532 (2011).
[52] As shown in Fig. 7, the calculations reveal a noticeable nonuniform variation of Q_a with $t'_\perp$ close to T_c that is at the base of the dome of negative values in the interval of $t'_\perp/k_B$ between 33 and 39 K and beyond $t'_\perp/k_B \simeq 43$ K in the positive sector. This nonuniform variation is not the result of additional quantum critical points in the phase diagram, as confirmed by the absence of any anomaly in the RG quantities. It is rather ascribed to critical effects close to a sizable T_c where interactions get relatively strong and weak-coupling RG and the energy derivative of the scattering time become less accurate.
[53] V. J. Emery, R. Bruinsma, and S. Barisic, Phys. Rev. Lett. **48**, 1039 (1982).
[54] P. Delhaes, C. Coulon, J. Amiell, S. Flandrois, E. Toreilles, J. Fabre, and L. Giral, Mol. Cryst. Liq. Cryst. **50**, 43 (1979).
[55] P. M. Grant, J. Phys. Colloq. **44**, C3-847 (1983).

[56] C. Coulon, P. Delhaes, S. Flandrois, R. Lagnier, E. Bonjour, and J. Fabre, J. Phys. (Paris) **43**, 1059 (1982).

[57] R. Laversanne, C. Coulon, B. Gallois, J. P. Pouget, and R. Moret, J. Phys. Lett. **45**, L393 (1984).

[58] T. Giamarchi, Physica B: Condensed Matter (Amsterdam, Neth.) **230–232**, 975 (1997).

[59] We have chosen an effective range of values for $t_\perp$ that is slightly lower than that of band calculations in order to incorporate the effect of the downward renormalization of $t_\perp$ that takes place at the approach of the Mott scale T_ρ. This effect is not taken into account by the present RG calculations at the one-loop level [23,34].

[60] B. J. Klemme, S. E. Brown, P. Wzietek, G. Kriza, P. Batail, D. Jérome, and J.-M. Fabre, Phys. Rev. Lett. **75**, 2408 (1995).

[61] K. Bechgaard, M. Carneiro, M. Olsen, F. B. Rasmussen, and C. S. Jacobsen, Phys. Rev. Lett. **46**, 852 (1981).

[62] It should be stressed here that experiments are performed under constant-pressure conditions, whereas the calculations are obtained at constant volume. For relatively soft materials like the organics, constant-volume corrections to the data may modify the actual temperature dependence for a transport quantity like the Seebeck coefficient (see, for example, Ref. [68]).

[63] C. Bourbonnais, F. Creuzet, D. Jérome, K. Bechgaard, and A. Moradpour, J. Phys. Lett. **45**, L755 (1984).

[64] J. Shinagawa, Y. Kurosaki, F. Zhang, C. Parker, S. E. Brown, D. Jérome, K. Bechgaard, and J. B. Christensen, Phys. Rev. Lett. **98**, 147002 (2007).

[65] N. Doiron-Leyraud, P. Auban-Senzier, S. R. de Cotret, C. Bourbonnais, A. Sedeki, D. Jérome, K. Bechgaard, and L. Taillefer, Eur. Phys. J. B **78**, 23 (2010).

[66] F. Creuzet, D. Jerome, C. Bourbonnais, and A. Moradpour, J. Phys. C **18**, L821 (1985).

[67] J. Moser, J. R. Cooper, D. Jérome, B. Alavi, S. E. Brown, and K. Bechgaard, Phys. Rev. Lett. **84**, 2674 (2000).

[68] J. Moser, M. Gabay, P. Auban-Senzier, D. Jérome, K. Bechgaard, and J. M. Fabre, Eur. Phys. J. B **1**, 39 (1998).